

Lawrence Berkeley National Laboratory

LBL Publications

Title

On the use of adjoints in the inversion of observed quasi-static deformation

Permalink

<https://escholarship.org/uc/item/27g4w60g>

Journal

Geophysical Journal International, 224(2)

ISSN

0956-540X

Authors

Vasco, DW

Mali, Gwyn

Publication Date

2020-11-20

DOI

10.1093/gji/ggaa481

Peer reviewed

On the use of adjoints in the inversion of observed quasi-static deformation

D. W. Vasco¹ and Gwyn Mali²

¹ *Lawrence Berkeley National Laboratory
University of California
Berkeley, California 94720*

² *Chevron North America Exploration and Production
Bakersfield, California 93311*

SUMMARY

An adjoint-based conjugate gradient algorithm provides an efficient means for imaging sources of deformation within the Earth, such as volume stresses associated with fluid flow in aquifers and reservoirs. For time intervals over which the overburden deforms elastically, one can calculate the gradient elements for a single model update using just two numerical simulations. The first is a forward run that is used to compute the residuals associated with the given iteration. The second simulation is to evaluate the application of the adjoint operator to the residuals. In this adjoint calculation, the residual displacements are applied as sources at the measurement locations, driving the deformation in the simulation. The volume stress on the source grid blocks, in response to the residual displacements, provide the gradient components. We apply this technique to satellite-based interferometric synthetic aperture radar (InSAR) line-of-sight displacements that were observed over an oil reservoir in California’s Central Valley. We find that the adjoint-based gradient estimates, requiring 18 CPU seconds, agree with conventional numerical calculations that take over 3700 CPU seconds to compute. Conjugate gradient algorithms utilizing the conventional approach and adjoint-based gradient computations give roughly the same reductions in misfit and similar final estimates of reservoir volume change.

Key words: Geomechanics, Radar interferometry, Inverse theory.

1 INTRODUCTION

In the past several decades, we have seen the development of techniques for obtaining large-scale and spatially-dense data sets that can be acquired repeatedly to monitor deformation-inducing processes, such as fluid flow. These include airborne and satellite-based methods such as interferometric synthetic aperture radar (InSAR) data (Ferretti 2014) and light detection and ranging (LiDAR) observations (Eitel et al. 2016), as well as time strains from repeated time-lapse seismic surveys (Hatchell & Bourne 2005; Tura et al. 2005; Staples et al. 2007; Hodgson et al. 2007). Correspondingly, advances in the numerical modeling of deformation in elastic, poroelastic, and general media have led to coupled simulators that include fluid flow, thermal processes, chemistry, along with geomechanics (Rutqvist et al. 2002; Kim et al. 2012). Such large data sets and advanced modeling tools require efficient methods for imaging sub-surface pro-

cesses using available high-density data and realistic Earth models.

Currently there are few examples of full-scale inversions for high-resolution aquifer or reservoir models. There are several reasons for the current shortage of successful inversions. First, large-scale coupled models can take days or even weeks for a single forward run, meaning that any inversion algorithm must be extremely efficient. Second, fully coupled models require a large number of parameters for their complete description. Parameters, such as the sub-surface mechanical and flow properties, typically vary spatially and are often poorly known and can trade-off. Third, the adjoint equations for fully coupled finite-element formulations of the forward problem can be complicated and difficult to program successfully. Here we take a more limited approach to imaging changes in an aquifer or reservoir due processes such as fluid injection and withdrawal, and simply determine

the effective volumetric stresses. That is, rather than taking the additional step of inferring the source of the volume change, which may be fluid pressure changes, temperature changes, chemical changes, or failure processes, we solve for the effect of the source volume on the surrounding medium. As indicated below, with these assumptions and the proper formulation, we can utilize an easily implemented adjoint expression for the calculation of the gradient and for model updating. In particular, the gradient may be obtained by two forward runs of a simulator, one to calculate the residuals, and a second one to evaluate the adjoint operator applied to the residuals. In this reciprocal calculation the residual displacements, applied at the measurement locations, drive the simulated deformation and the resulting changes in the volume stresses within the source grid blocks provide the gradient components. We illustrate this approach with an application to a set of interferometric synthetic aperture range change observations from a reservoir in the Central Valley of California.

Other approaches utilizing adjoints for inverse problems include early work in the inversion of fluid pressure observations (Jacquard & Jain 1965) and more closely related work in seismic imaging presented (Tarantola 1984; Tarantola 1988). Applications to inverse problems in static elasticity (Oberai et al. 2003) and poroelasticity (Lecampion & Constantinescu 2005; Iglesias & McLaughlin 2012; Hesse & Stadler 2014), have focused on the nonlinear problem of estimating model constitutive parameters such as permeability. In this work we shall deal with the determination of the source of deformation, which is a linear problem. Previous studies have addressed the problem of source estimation (Kaderli et al. 2018), but the vast majority of that work involves the dynamic problem associated with the propagation of elastic waves, adding the additional complication of temporal variation. Typically, such studies also include the source location as an unknown, again leading to a nonlinear inverse problem. Because we are limiting our scope to the estimation of an effective source using static or quasi-static deformation data, the approach described here is simpler than these earlier methods. Furthermore, the technique is easy to implement, even for large geologically complex models, and in many cases it does not require extensive re-coding.

2 METHODOLOGY

2.1 Governing Equations

Our starting point is the equation governing displacements in a linear elastic medium due to sources of deformation within the Earth. For an anisotropic elastic medium, characterized by the 21 elastic parameters $c_{ijkl}(\mathbf{x})$ and density $\rho(\mathbf{x})$, the components of the displacement vector $\mathbf{u}(\mathbf{x}, \omega)$ at a point \mathbf{x} and at frequency ω are governed by

$$\rho\omega^2 u_i - \frac{\partial}{\partial x_j} \left(c_{ijkl} \frac{\partial u_k}{\partial x_l} \right) = \Sigma_i(\omega) \quad (1)$$

where $\Sigma_i(\omega)$ signifies the i -th component of the source function. In what follows we will consider quasi-static or static deformation, where ω is assumed to be small or zero. An alternative formulation, that has some advantages both numerically and in specifying the boundary conditions, frames

the problem in terms of both the displacements, u_i , and the stresses, σ_{ij} . In the time-domain the governing equations are

$$\sigma_{ij} = c_{ijkl} \frac{\partial u_k}{\partial x_l} \quad (2)$$

$$\rho \frac{\partial^2 u_i}{\partial t^2} = \frac{\partial \sigma_{ij}}{\partial x_j} + \Sigma_i(t) \quad (3)$$

along with appropriate boundary conditions which are typically zero normal stress at the Earth's surface and vanishing displacements on the interior boundaries. For a general heterogeneous medium the governing equation (1), or equations (2) and (3), are solved numerically using an approach such as finite-differences, finite-volume (Bailey & Cross 1995; Fallah et al. 2000), or finite-elements (Igel 2017).

As shown in Appendix A, there is an alternative integral formulation that relates the measurements at observation point \mathbf{x}_i , $d(\mathbf{x}_i)$, to changes in the source region S_σ . Because we are interested in deformation due to fluid volume changes at depth, we assume that the displacements are induced by volumetric stress changes, leading to surface tractions, \mathbf{T} , at the reservoir boundaries. The integral expression relating the magnitudes of changes in these surface tractions $T(\boldsymbol{\xi})$ to range change observed at the Earth's surface, $d(\mathbf{x}_k)$ is

$$d(\mathbf{x}) = \int_{S_\sigma} T(\boldsymbol{\xi}) K(\mathbf{x}, \boldsymbol{\xi}) d\boldsymbol{\xi}. \quad (4)$$

where the kernel of the integral operator is defined in terms of the components of the satellite look vector \mathbf{l} and the normal to the surface, $\mathbf{n}(\boldsymbol{\xi})$

$$K(\mathbf{x}, \boldsymbol{\xi}) = n_i l_k G_{ki}(\mathbf{x}, \boldsymbol{\xi}) \quad (5)$$

and $G_{ki}(\mathbf{x}, \boldsymbol{\xi})$ is the Green's function providing the response of the medium to a point force (Aki and Richards 1980). We can obtain a discrete inverse problem by sub-dividing the source surface S_σ into a collection of M patches and considering the effective normal traction on each patch, m_l . The integral then reduces to a sum

$$d(\mathbf{x}_k) = \sum_{l=1}^M A_{kl} m_l \quad (6)$$

where the coefficients are defined in terms of integrals over each surface patch, S_l ,

$$A_{kl} = \int_{S_l} K(\mathbf{x}_k, \boldsymbol{\xi}) d\boldsymbol{\xi}. \quad (7)$$

A more comprehensive discussion on the discretization of the forward problem is provided in Appendix A.

The differential and integral formulations are mathematically equivalent as long as the boundary conditions and source specifications are the same. Thus, if the numerical methods for solving each class of equations is properly implemented they should give the same results. In fact, numerical methods for solving the governing differential equations are often used to calculate the response of the elastic system to volumetric stress changes in a single grid block or tractions on a grid block's surfaces, the impulse response integrated over a grid block or a surface element.

2.2 The Inverse Problem and a Conjugate Gradient Solution

For the forward problem we simply compute the range change at the Earth's surface due to a given distribution of normal stress changes acting upon the reservoir boundaries. The solution to the forward problem is obtained by either solving the differential equation (1) or by evaluating a set of integrals in the form of equation (4) or its discrete equivalent (6). In the inverse problem we are given a collection of N observed data, which we denote by the vector $\mathbf{d} = [d(\mathbf{x}_1), d(\mathbf{x}_2), \dots, d(\mathbf{x}_N)]$, from a particular area of interest and seek to determine the volumetric stresses at depth that best explain the observations. For linear inverse problems with observations subject to errors that are assumed to follow an approximately Gaussian distribution, the well established least squares approach is usually adopted (Menke 2018), whereby one minimizes the sum of the squares of the residuals,

$$J(\mathbf{m}) = \frac{1}{2} (\mathbf{d} - \mathbf{A}\mathbf{m})^T (\mathbf{d} - \mathbf{A}\mathbf{m}), \quad (8)$$

which we have written in vector-matrix notation. Due to the smoothing nature of the integral expression (4), the minimum of $J(\mathbf{m})$ is sensitive to errors in the observations unless care is taken to stabilize or regularize the minimization algorithm (Parker 1994; Aster 2013; Menke 2018). The most common form of regularization for least squares-based inversions involves the addition of quadratic terms penalizing some undesirable aspect of the solution, such as model roughness or the norm of deviations from a prior model (Menke 2018). There are a variety of penalty terms that may be incorporated into an inversion algorithm. As an illustration that will prove useful in our application, we will adopt a simple function that penalizes deviations from estimates of pressure changes, \mathbf{p} , based upon well observations,

$$P(\mathbf{m}) = \sum_{i=1}^M (m_i - \alpha p_i)^2, \quad (9)$$

where α is a scaling factor relating pressure change to surface traction on S_σ . Thus, the total misfit functional is given by

$$Q(\mathbf{m}) = J(\mathbf{m}) + w_p P(\mathbf{m}) \quad (10)$$

where w_p is a weighting factor that determines the importance of the regularization relative to the misfit functional. As shown below, the simple quadratic forms of the terms in equation (10) allows for an analytic expression for the minimum of the penalized misfit functional (10). However, to formulate the quadratic form $Q(\mathbf{m})$ we need to calculate the elements of the matrix \mathbf{A} , the impulse responses or sensitivities. The calculation of each column of \mathbf{A} requires one forward run of a numerical simulator, meaning that M simulator runs will be required, where M is the number of grid blocks representing the source. For the Central Valley simulation described below, 900 simulations were required in order to construct \mathbf{A} . For large models, tens of thousands to millions of simulations might be needed to construct \mathbf{A} explicitly.

The conjugate gradient algorithm offers an alternative to an explicit solution. This iterative approach starts with an initial model \mathbf{m}_0 and successively updates the model,

using the gradient of the functional $Q(\mathbf{m})$, that is the partial derivatives with respect to model parameters

$$(\nabla Q)_i = \frac{\partial Q}{\partial m_i}, \quad (11)$$

to determine the update at each step (Gill et al. 1982; Dorny 1983)

$$\mathbf{m}_n = \mathbf{m}_{n-1} + \alpha_{n-1} \nabla Q(\mathbf{m}_{n-1}). \quad (12)$$

The step length or magnitude of the update, α_{n-1} , is determined by a line search in the direction of the gradient. It is certainly possible to forgo the line search and pick a step length based upon properties of the gradient (Gill et al. 1982). Such techniques tend to have slower convergence that may result in more iterations, negating the computational savings in forward simulations at each iteration. The conjugate gradient algorithm is perhaps the simplest of a class of iterative approaches, such as the limited memory quasi-Newton method, (Byrd et al. 1995). However, for our purposes it serves to illustrate how an approach based upon adjoints can provide an efficient means for inverting extensive data sets for models containing a large number of parameters.

2.3 Adjoint-Based Gradient Computation

Typically, the most computationally intensive step of the conjugate gradient algorithm is the calculation of the components of the gradient. If a direct perturbation approach is adopted, whereby one perturbs each of the N parameters in succession and computes a numerical derivative, then $N + 1$ forward simulations are required. For models that must be represented on a large mesh, N can range from hundreds of thousands to millions of parameters. Here we describe a different technique for calculating the gradient components that relies on the solution of the adjoint equation. Employing this methodology, coupled with the conjugate gradient algorithm, two forward simulations are required for each gradient calculation and a handful more are required for the line search, if one is employed. As noted by (Gill et al. 1982), the conjugate gradient algorithm could require as many as N iterations in order to reach a minimum, eliminating any advantage of our approach. However, in practice the algorithm converges rapidly to a minimum, particularly for the quadratic function associated with our linear least squares problem.

For a discrete problem, such as the one formulated using a numerical simulation grid in equation (6), we can provide a simple derivation of the model parameter gradient in terms of the adjoint of the operator \mathbf{A} that defines the forward problem

$$\mathbf{d} = \mathbf{A}\mathbf{m}, \quad (13)$$

where \mathbf{d} are the calculated displacements at points in the model grid and \mathbf{m} are the model parameters. Note that, this is just equation (6) written in vector-matrix form. In our case the model parameters specify the strength of the source in the numerical simulation and may represent quantities such as the normal tractions related to volume changes in the source grid blocks or aperture changes on fault/fracture patches. A more formal derivation of the gradient in terms

of the adjoint operator is provided in Appendix B, based upon the work of (Plessix 2006).

For the moment, let us consider the inverse problem without the regularization penalty terms. Thus, the misfit functional is given by the expression for the sum of the squares of the residuals

$$J(\mathbf{m}) = \frac{1}{2} (\mathbf{d} - \mathbf{A}\mathbf{m})^T (\mathbf{d} - \mathbf{A}\mathbf{m}). \quad (14)$$

Taking the gradient of $J(\mathbf{m})$ with respect to the model parameters \mathbf{m} results in an expression that is linear in the model parameters

$$\nabla_m J(\mathbf{m}) = -\mathbf{A}^T (\mathbf{d} - \mathbf{A}\mathbf{m}). \quad (15)$$

In the direct approach, this linear equation is set equal to zero, producing a necessary condition for the minimum of $J(\mathbf{m})$, and solved for \mathbf{m} . That allows one to obtain the solution without the iterative minimization necessary in the conjugate gradient algorithm. Unfortunately, such an approach requires the calculation of the entries of the matrix \mathbf{A} which are dependent on the Green's functions and the repeated solution of the forward problem. However, noting that, for a given model \mathbf{m} , the quantity in brackets is the residual vector

$$\mathbf{r} = \mathbf{d} - \mathbf{A}\mathbf{m} \quad (16)$$

and the gradient is given by

$$\nabla_m J(\mathbf{m}) = -\mathbf{A}^T \mathbf{r} \quad (17)$$

we can derive an alternative expression for the gradient. For a linear matrix operator the transpose is equal to the adjoint operator (Dorny 1983), defined as the matrix \mathbf{A}^* such that

$$\langle \mathbf{A}\mathbf{x}, \mathbf{y} \rangle = \langle \mathbf{x}, \mathbf{A}^* \mathbf{y} \rangle \quad (18)$$

where \mathbf{x} and \mathbf{y} are vectors and $\langle \mathbf{x}, \mathbf{y} \rangle$ denotes the inner or scalar product that is also given as $\mathbf{x} \cdot \mathbf{y}$ and $\mathbf{x}^T \mathbf{y}$. Given the equivalence of the transpose, \mathbf{A}^T , and the adjoint, \mathbf{A}^* , we may write the gradient as the adjoint operator applied to the residual vector

$$\nabla_m J(\mathbf{m}) = -\mathbf{A}^* \mathbf{r}. \quad (19)$$

A second formulation leading to equation (19) is provided in Appendix B, following the approach of (Plessix 2006). In that derivation we do not invoke the equivalent of the adjoint and the transpose. Utilizing the adjoint of the kernel in equation (4) we can write the components of the gradient as

$$\frac{\partial J(\mathbf{m})}{\partial m_j} = - \int_S K^*(\mathbf{x}, \boldsymbol{\xi}_j) r(\mathbf{x}) d\mathbf{x} \quad (20)$$

where $\boldsymbol{\xi}_j$ is the center of the j -th surface element, for example the top surface of the j -th grid block representing the reservoir, $r(\mathbf{x})$ are the residuals distributed over the observation locations, which may be the Earth's surface in the case of InSAR data or a volume of overburden in the case of time-lapse seismic strain (Tura et al. 2005). Equation (20) states that the gradient can be obtained by applying the adjoint operator to the residual vector.

While we can calculate the integrals (20) in a straightforward fashion when suitable Green's functions are available, computing Green's functions for a fully three-dimensional elastic model can be time consuming. It is possible to evaluate the integral in equation (20) much more

efficiently from a single run of a numerical simulator, such as a finite-difference code for solving equation (1). In particular, using equations (A16) and (A17) in Appendix A, relating the Green's function and its adjoint, one can show that the quantity on the right-hand-side of equation (20) is equivalent to the forward problem with the residuals applied as sources at the observation points. The resulting normal stresses acting on the boundary of the grid block that coincides with a patch of the source surface S_σ , provides the component of the gradient associated with that surface element. An approach based upon a finite-difference simulation is likely to be the most common technique for implementing equation (19). For example, we have an implicit finite-difference program for solving the static version of equation (1) where ω is assumed to be zero. In addition, we have a time-stepping code for solving equations (2) and (3) for a slowly varying source that can be used to determine the displacements and stresses due to specified sources. In the applications section we use the latter code to calculate the gradients using equation (20) and compare these estimates with a conventional approach (Vasco & Ferretti 2005). As noted in (Kaderli et al. 2018), the displacement-stress formulation can be brought into a self-adjoint form through a simple scaling of the dependent variables, leading to a scaled source for the adjoint equation.

3 APPLICATION

3.1 Monitoring Reservoir Production and Injection using Interferometric Synthetic Aperture Radar Observations

In this section, we apply the methodology to interferometric synthetic aperture radar (InSAR) gathered over an active oil field in the Central Valley of California. Due to the compressible nature of the reservoir, there is significant surface deformation associated with injection and production over intervals of one month (Vasco et al. 2017). Our goal is to determine the distribution of normal stresses on S_σ on the reservoir upper boundary that can best explain the observed range change. We adopt the conjugate gradient algorithm (12) in order to successively update the source model of the normal stresses generated by fluid volume changes in order to produce predictions that better match the observations. The misfit functional (10) contains the data misfit term $J(\mathbf{m})$ and the penalty term $P(\mathbf{m})$. Before we discuss the details of the inversion we compare the conventional perturbation approach for gradient calculations with an approach based upon the adjoint algorithm described above.

3.2 Examples of Gradient Calculations

Our initial gradient calculations were based upon an approach used in previous studies (Vasco & Ferretti 2005; Rucci et al. 2010; Vasco et al. 2010; Vasco et al. 2017), where each individual source grid block at the upper boundary of the reservoir is used as a source of deformation. For general three-dimensional elastic models we use a numerical finite-difference code to solve for the static or quasi-static displacements (Vasco et al. 2017) at each observation point that results from successively treating each grid block as a

source. Thus, one must run the forward problem for each of these grid blocks in order to compute the gradient vector. For most models with source representations involving many hundreds to a few thousand grid blocks or fault patches, such calculations take of the order of 1 to 10 hours.

For the reservoir model considered here, described by variations on a 30 (x) by 30 (y) by 20(z) grid, there were a total of 18,000 grid blocks with a grid block size of 100 m. The grid covered the anticline that defines the field, shown in Figure 1, but does not provide extensive coverage beyond the structure due to data limitations. Therefore, the boundaries of our grid are somewhat closer to our estimate locations than we would like, but that is a realistic limitation in many areas. The source layer was composed of 900 blocks defined by the reservoir upper boundary. Therefore 900 forward simulations of the finite-difference code were required for a complete set of sensitivity calculations, in order to define the matrix \mathbf{A} in the term $J(\mathbf{m})$ given by equation (8) and \mathbf{A}^T in equation (17). The boundary conditions are zero displacements at the edges of the model. It was necessary to extend the model above the Earth’s surface by including an overlying atmospheric layer in order to satisfy the boundary condition at the top of the model.

Two distinct variations in properties were considered, in order to capture the influence of spatial variations in the elastic model on the gradient calculations. First, we averaged all of the grid block properties of a three-dimensional elastic model of the region, generating a uniform medium with a bulk modulus of 1.35 GPa, a shear modulus of 1.14 GPa, and a density of 1757.8 kg/m³. As a baseline, we computed the components of the gradient vector using a conventional perturbation approach, perturbing the normal stress on the grid block at the reservoir upper boundary and calculating the resulting range changes at the observation points on the surface are calculated. Numerical differencing of the perturbed and unperturbed simulation results are then used to compute each gradient component. The 901 forward simulations for the conventional gradient calculation required 61.8 minutes, or 3710 seconds, of CPU time for the sensitivity calculation. From equation (17) it is clear that the gradient components are a linear mapping of the residuals. For reference, we include a plot of the residual vectors for the first three iterations of the conjugate gradient algorithm (Figure 2). The resulting numerical gradient components for set of source grid blocks comprising the reservoir upper boundary are shown in the central panel in Figure 3, plotted in their respective locations. As expected, the numerical gradient clearly resembles a negative image of the residuals.

For comparison with the numerical result, we also computed the gradient components using the adjoint approach, based upon equation (20). Specifically, we averaged the line-of-sight displacement residuals (Figure 2) over each grid element at the surface of the model and then applied the displacement as a source at the grid block center. The components of the gradient for this case were obtained after only 18 CPU seconds of computation. The resulting normal stress on the grid block face corresponding to a patch of the reservoir boundary, or the equivalent volumetric stress change within the appropriate grid block, provides the gradient components which are plotted in the center panel of Figure 3. There is generally good agreement between these estimates and the conventional numerical estimates. To quantify the

disagreement, we plot the differences between the calculated numerical and adjoint gradients, at the same scale as these estimates in the right-most panel of Figure 3. The pattern of residuals changes with each update, as shown in Figure 2, with a general reduction in the magnitude of the residuals as the model evolves and the fit improves, leading to changes in the gradient components (Figures 4 and 5). Again, there is fairly good agreement between the conventional and the adjoint-based gradient components and the differences are much smaller than the gradient magnitudes.

To understand the influence of laterally-varying material properties, we considered a full three-dimensional model. The depth to the top boundary of the reservoir and a horizontal section through the model are plotted in Figure 1. There are significant variations in the bulk modulus with depth, from less than 0.2 GPa to over 1.7 GPa at a depth of more than 0.8 km. In Figure 6 the conventional and adjoint gradient components for the initial iteration of the conjugate gradient algorithm are plotted for this heterogeneous example. There is large-scale agreement between the two sets of calculated values and their magnitudes are similar, and significantly larger those associated with the uniform model shown in Figure 3. As is evident in Figure 1, the model contains abrupt variations in material properties which may be responsible for the small-scale differences between the two gradient estimates. The difference between the two gradient estimates is larger than in the case of the homogeneous medium (Figure 3) and the pattern of discrepancies is somewhat more variable in space.

3.3 Application of the Conjugate Gradient Algorithm

In this sub-section we apply the conjugate gradient algorithm (12) to minimize the penalized misfit functional $Q(\mathbf{m})$ given by equation (10). The weight w_p was set at 3.0×10^{-5} , based upon a combination of trial and error inversions and a trade-off curve calculation. For the adjoint-based approach the gradient is calculated using the expression

$$\nabla_m Q(\mathbf{m}) = -\mathbf{A}^* \mathbf{r} + 2w_p (\mathbf{m} - \alpha \mathbf{p}), \quad (21)$$

requiring two simulations per iteration of the algorithm, while 901 simulations were used in the conventional numerical calculations. The total misfit reduction for both inversions levels off after a total of 10 iterations (Figure 7) and the final error reduction and the fit to the observations are quite similar for both techniques (Figure 8). The line search added around 2-8 forward runs per iteration, so that the adjoint-based algorithm required at most 105 total simulations, almost an order of magnitude fewer than the conventional approach. It is possible to dispense with the line search and to approximate the step size using other means, further reducing the number of simulations required (Press et al. 1992). However, that could increase the number of conjugate gradient updating iterations needed to fit the data. The final models for the two approaches, shown in Figure 9, are very similar and indicate the most significant volumetric stress changes beneath the peak of range change in Figure 2 but shifted to the east, likely due to the look angle of the InSAR data. The differences, obtained by a direct subtraction of the adjoint-based conjugate gradient solution from the numerical conjugate gradient solution are relatively small in

comparison with the estimates. Though the approach works best for a dense data set, such as InSAR range changes, it can also be used for a sparse set of measurements. For example, we decimated the range change data shown in Figure 2, re-interpolating onto a 20 by 20 grid of values, many fewer observations than the 2986 values considered above. An adjoint-based inversion with this sparse data set still produces a solution that resembles the solution produced by the conjugate gradient algorithm utilizing the numerical gradient (Figure 10). Note that the overall amplitude of the solutions are reduced in size in comparison to the inversion of the denser set of values. This is likely due to the fixed penalty weighting factor and a data misfit function that is much smaller due to the many fewer observations used in the inversion. This effect can be mitigated by re-weighting the penalty function based upon data size.

4 DISCUSSION AND CONCLUSIONS

The adjoint-based inversion methodology appears to be a promising approach for imaging sources of quasi-static deformation within the Earth, such as aquifer/reservoir volume changes due to fluid injection and withdrawal. The technique, as presented in this paper, only requires numerical solutions of the equations governing elastic deformation during a time-interval of interest. Because we treat the reservoir as a source of deformation and solve for the effective properties of the source, such as the surface traction due to volumetric stress changes within the reservoir, we make no assumptions regarding the internal processes with the source grid blocks. Using such an effective source is both a strength and a limitation of our approach. One advantage of this formulation is that we need to make very few assumptions about the behavior of the medium and only require the elastic properties of the overburden to invert for the areas of volume change within the source region. In this approach one does not have to model processes such as fluid pressure changes, thermal effects, the mechanical breakdown of the medium, or chemical effects. Thus, we do not need the coupling coefficients such as poroelastic parameters in order to estimate the source strain. Such coefficients are likely to vary spatially and can trade-off with quantities of interest, such as the magnitude of fluid pressure change (Rucci et al. 2010).

The philosophy that we adopt is to use the geophysical monitoring data to estimate temporal and spatial variations in the source volumetric stress changes and to use these changes to try and understand the controlling features in an aquifer or reservoir, such as a permeable fracture zone or a barrier to flow. If we have a number of temporal snapshots of the changes in the source volume and we can relate the changes to a specific cause, such as fluid pressure changes, one may estimate reservoir/aquifer permeability using an onset time technique that is not very sensitive to the intervening rock physics model (Rucci et al. 2010). The onset time methodology is general and may be applied to general time-lapse geophysical data sets for which the temporal variations are controlled by fluid flow (Vasco et al. 2014).

One disadvantage of the limited interpretation of changes within the source region is that we cannot take full advantage of additional observations such as well pressure data. That is, we cannot use the physics of coupled flow to

relate utilize well pressure changes and reservoir deformation in a direct fashion. Rather, we have to constrain the estimates using a less direct approach such as distance constraints from wells (Vasco et al. 2019) or volume constraints from injection and production data (Vasco et al. 2017), such as the penalty term $P(\mathbf{m})$ in equation (10). It is possible to use this formulation in coupled simulators, such as those employing finite-elements to solve the set of equations governing coupled fluid flow and geomechanics. However, the adjoint problem is more involved when the equations deviate from linear elasticity. Solving these more involved problems will be the subject of future research. In addition, we will consider significantly larger problems, such as those involving hydrological basins tens to hundreds of kilometers in extent (Vasco et al. 2019).

ACKNOWLEDGMENTS

This material is based upon work supported by the U.S. Department of Energy, Office of Science, Office of Basic Energy Sciences, Chemical Sciences, Geosciences, and Biosciences Division under contract number DE-AC02-05-CH11231 and Chevron. Work performed on the InSAR data from the Central Valley field was supported by Chevron.

REFERENCES

- Aki, K. & Richards, P. G., 1980. *Quantitative Seismology*, Freeman and Sons, San Francisco.
- Aster, R. C., Borchers, B., & Thurber, C., 2013. *Parameter Estimation and Inverse Problems*, Academic Press, San Diego.
- Backus, G., & Mulcahy, M., 1976. Moment tensors and other phenomenological descriptions of seismic sources - I. Continuous displacements, *Geophysical Journal of the Royal Astronomical Society*, **46**, 341–361.
- Bailey, C. & Cross, M., 1995. A finite volume procedure to solve elastic solid mechanics problems in three dimensions on an unstructured mesh, *International Journal for Numerical Methods in Engineering*, **38**, 1757–1776.
- Byrd, R. H., Lu, P., Nocedal, J., & Zhu, C., 1995. A limited memory algorithm for bound constrained optimization, *SIAM Journal of Scientific Computing*, **16**, 1190–1208.
- Castellanos, C., Etienne, V., Hu, G., Oporto, S., Brossier, R., & Virieux, J., 2011. Algorithmic and methodological developments towards full wave-form inversion in 3D elastic media, in *81st Annual Meeting*, pp. 2793–2797, Society of Exploration Geophysicists.
- Dorn, C. N., 1983. *A Vector Space Approach to Models and Optimization*, Robert E. Krieger Publishing Company, Malabar, Florida.
- Eitel, J. U., Hlflé, H. B., Vierling, L. A., Abellan, A., Asenr, G. P., Deems, J. S., & Glennie, C. L., 2016. Beyond 3-D: The new spectrum of LiDAR applications for earth and ecological sciences, *Remote Sensing of Environment*, **186**, 372–392.
- Fallah, N. A., Bailey, C., Cross, M., & Taylor, G. A., 2000. Comparison of finite element and finite volume methods application in geometrically nonlinear stress analysis, *Applied Mathematical Modeling*, **24**, 439–455.
- Ferretti, A., 2014. *Satellite InSAR Data: Reservoir Monitoring from Space*, European Association of Geoscientists and Engineers.
- Gill, P. E., Murray, W., & Wright, M. H., 1982. *Practical Optimization*, Academic Press, New York.
- Hatchell, P. & Bourne, S., 2005. Rocks under strain: Strain-induced time-lapse time-shifts are observed for depleting reservoirs, *The Leading Edge*, **24**, 1234–1242.
- Hesse, M. A. & Stadler, G., 2014. Joint inversion in coupled quasi-static poroelasticity, *Journal of Geophysical Research*, **119**, 1425–1445.
- Hodgson, N., MacBeth, C., Duranti, L., Rickett, J., & Nihei, K., 2007. Inverting for reservoir pressure changes using time-lapse time strain: Application to the Genesis field, Gulf of Mexico, *The Leading Edge*, **26**, 649–652.
- Igel, H., 2017. *Computational Seismology - A Practical Introduction*, Oxford University Press, Oxford.
- Ichihara, M., Kusakabe, T., Kame, N., & Kumagai, H., 2016. On volume-source representations based on the representation theorem, *Earth, Planets and Space*, **68**, 1–10.
- Iglesias, M. A. & McLaughlin, D., 2012. Data inversion in coupled sub-surface flow and geomechanics models, *Inverse Problems*, **28**.
- Jacquard, P., & Jain, C., 1965. Permeability distribution from field pressure data, *Society of Petroleum Engineering Journal*, **5**, 281–294.
- Kaderli, J., McChesney, M. D., & Minkoff, S. E., 2018. A self-adjoint velocity-stress full-waveform inversion approach to microseismic source estimation, *Geophysics*, **83**, R413–R427.
- Kim, J., Sonnenthal, E. L., & Rutqvist, J., 2012. Formulation and sequential numerical algorithms of coupled fluid/heat flow and geomechanics for multiple porosity materials, *International Journal for Numerical Methods in Engineering*, **92**, 425–456.
- Komatitsch, D. & Tromp, J., 1999. Introduction to the spectral-element method for 3-D seismic wave propagation, *Geophysical Journal International*, **139**, 806–822.
- Lecampion, B. & Constantinescu, A., 2005. Sensitivity analysis for parameter identification in quasi-static poroelasticity, *International Journal for Numerical and Analytical Methods in Geomechanics*, **29**, 163–185.
- Menke, W., 2018. *Geophysical Data Analysis: Discrete Inverse Theory*, Academic Press, London.
- Oberai, A. A., Gokhale, N. H., & Feijoo, G. R., 2003. Solution of inverse problems in elasticity imaging using the adjoint method, *Inverse Problems*, **19**, 297–313.
- Parker, R. L., 1994. *Geophysical Inverse Theory*, Princeton University Press, Princeton.
- Plessix, R.-E., 2006. A review of the adjoint-state method for computing the gradient of a functional with geophysical applications, *Geophysical Journal International*, **167**, 495–503.
- Press, W. H., Teukolsky, S. A., Vetterling, W. T., & Flannery, B. P., 1992. *Numerical Recipes*, Cambridge University Press, Cambridge.
- Roach, G. F., 1970. *Green's Functions - Introductory Theory with Applications*, Van Nostrand-Reinhold Company, London.
- Rucci, A., Vasco, D. W., & Novali, F., 2010. Fluid pressure arrival time tomography: Estimation and assessment in the presence of inequality constraints, with an application to production at the Krechba field, Algeria, *Geophysics*, **75**, O39–O55.
- Rutqvist, J., Wu, Y.-S., Tsang, C.-F., & Bodvarsson, G. A., 2002. Modeling approach for analysis of coupled multiphase fluid flow, heat transfer, and deformation in fractured porous rock, *International Journal of Rock Mechanics and Mining Science*, **39**, 429–442.
- Stakgold, I., 1979. *Green's Functions and Boundary Value Problems*, John Wiley and Sons, New York.
- Staples, R., Ita, J., Burrell, R., & Nash, R., 2007. Monitoring pressure depletion and improving geomechanical models of the Shearwater field using 4D seismic, *The Leading Edge*, **26**, 636–642.
- Tarantola, A., 1984. The seismic reflection inverse problem, in *Inverse Problems of Acoustic and Elastic Waves*, F. Santosa, Y., Pao, W. W. Symes, and C. Holland, (Eds.), Siam, Philadelphia.
- Tarantola, A., 1988. Theoretical background for the inversion of seismic waveforms, including elasticity and attenuation, *Pure and Applied Geophysics*, **128**, 365–399.
- Tura, A., Barker, T., Cattermole, P., Collins, C., Davis, J., Hatchell, P., Koster, K., & Schutjens, P. adn Wills, P., 2005. Monitoring primary depletion reservoirs using amplitudes and time shifts from high-repeat seismic surveys, *The Leading Edge*, **24**, 1214–1221.
- Vasco, D. W. & Ferretti, A., 2005. On the use of quasi-static deformation to understand reservoir fluid flow, *Geophysics*, **70**, O13–O27.
- Vasco, D. W., Rucci, A., Ferretti, A., Novali, F., Bissell, R., Ringrose, P., Mathieson, A., & Wright, I., 2010. Satellite-based measurements of surface deformation reveal flow flow associated with the geological storage of carbon dioxide, *Geophysical Research Letters*, **37**, 1–5.
- Vasco, D. W., Daley, T. M., & Bakulin, A., 2014. Utilizing the onset of time-lapse changes: a robust basis for reservoir monitoring and characterization, *Geophysical Journal International*, **197**, 542–556.
- Vasco, D. W., Harness, P., Pride, S., & Hoversten, M., 2017. Estimating fluid-induced stress changes from observed deformation, *Geophysical Journal International*, **208**, 1623–1642.
- Vasco, D. W., Farr, T. G., Jeanne, P., Doughty, C., & Nico, P., 2019. Satellite-based monitoring of groundwater depletion in California's Central Valley, *Scientific Reports*, **9**, 16053.

5 APPENDIX A: GREEN'S FUNCTIONS, A SOURCE REPRESENTATION, AND THE DISCRETE INVERSE PROBLEM

5.1 Green's functions and their adjoints

Here we derive an explicit expression for the range change at the free surface in terms of volumetric stress changes in a source region at depth. For brevity we denote i -th component of the linear vector differential operator given by the left-hand-side of equation (1) as

$$\mathcal{L}_i(\mathbf{u}) = \rho\omega^2 u_i - \frac{\partial}{\partial x_j} \left(c_{ijkl} \frac{\partial u_k}{\partial x_l} \right), \quad (A1)$$

for $i = 1, 2, 3$. The Green's function, or impulse response for a source in the direction of the positive n axis at the position $\boldsymbol{\xi}$, $\mathbf{G}_n(\mathbf{x}, \boldsymbol{\xi})$ satisfies the equation (Aki and Richards 1980)

$$\mathcal{L}_i(\mathbf{G}_n) = \delta_{in} \delta(\mathbf{x} - \boldsymbol{\xi}) \quad (A2)$$

where δ_{in} is the Kronecker delta function that equals 1 if $i = n$ and is zero otherwise. The impulse or delta function $\delta(\mathbf{x} - \boldsymbol{\xi})$ equals 1 when $\mathbf{x} = \boldsymbol{\xi}$ and vanishes everywhere else. The differential equation is also subject to boundary conditions which can be written in the abbreviated form

$$\mathcal{B}(\mathbf{u}) = 0 \quad (A3)$$

where \mathcal{B} is the boundary operator.

In what follows we shall need the adjoint of the differential operator \mathcal{L} , denoted by \mathcal{L}^* and defined by the condition

$$\langle \mathcal{L}(\mathbf{u}), \mathbf{v} \rangle = \langle \mathbf{u}, \mathcal{L}^*(\mathbf{v}) \rangle \quad (A4)$$

(Stakgold 1979), where the angle brackets signify the inner product

$$\langle \mathbf{u}, \mathbf{v} \rangle = \int_V \mathbf{u}(\boldsymbol{\xi}) \cdot \mathbf{v}(\boldsymbol{\xi}) dV \quad (A5)$$

(Roach 1970). Adjoint boundary conditions typically accompany the formal adjoint differential operator. We shall denote such boundary conditions as the vanishing of the adjoint boundary operator $\mathcal{B}^*(\mathbf{u})$. We can define an adjoint Green's function as the solution to the differential equation

$$\mathcal{L}_i^*(\mathbf{G}_n^*) = \delta_{in} \delta(\mathbf{x} - \boldsymbol{\xi}). \quad (A6)$$

A discussion of Green's functions and adjoints associated with second order differential operators is given in (Stakgold 1979). The Green's function and its adjoint for the linear vector differential operator \mathcal{L}_i are related by

$$G_{in}^*(\mathbf{x}, \boldsymbol{\xi}) = G_{ni}(\boldsymbol{\xi}, \mathbf{x}). \quad (A7)$$

Note that this relationship holds in general, even if the operator \mathcal{L}_i is not self-adjoint. That is, it holds even if the adjoint operator does not equal the original operator. If the operators are self-adjoint, as the operator for displacement formulation of linear elasticity is, and satisfy homogeneous boundary conditions, then one arrives at the principle of reciprocity (Aki and Richards 1980). Other numerical formulations may not be self-adjoint. For example, an approach based upon velocity and stress variables (Kaderli et al. 2018) is not self-adjoint unless a transformation developed by (Castellanos et al. 2011) is applied. From equation (A7) we conclude that one only has to solve the forward problem for $(\mathbf{G}_n)_i(\mathbf{x}, \boldsymbol{\xi})$ and then interchange \mathbf{x} and $\boldsymbol{\xi}$ and the indices i and n in order to obtain the adjoint Green's

function. Thus, the observation locations become the source locations and the components contributing to the observations now contribute to the source. Conversely, the components contributing to the source are now used to define the observed values.

5.2 A representation of the source

Consider deformation-inducing processes acting throughout a source volume V_σ , such as an aquifer or a reservoir. These activities may involve fluid volume changes, thermal and chemical effects, and may even be characterized by inelastic and nonlinear behavior. However, as noted by (Aki and Richards 1980), if one surrounds the source volume by a surface S_σ that is sufficiently far from the non-elastic behavior so that the deformation is elastic, one can represent the effect of the possible non-linear processes by a distribution of displacements \mathbf{u} and tractions $\boldsymbol{\tau}$ over the surface

$$u_k(\mathbf{x}) = - \int_{S+S_\sigma} c_{ijpq} u_i n_j \frac{\partial G_{kp}}{\partial \xi_q} d\xi + \int_{S+S_\sigma} \tau_i G_{ki} d\xi, \quad (A8)$$

where $n_j(\boldsymbol{\xi})$ are the components of the normal to the surface and we have included the external surface, S , because it can also come into play. As is discussed in Ichihara et al. (2016), it is possible to rewrite the representation (A8) solely in terms of a distribution of tractions over the surfaces

$$u_k(\mathbf{x}) = \int_{S+S_\sigma} T_i G_{ki} d\xi, \quad (A9)$$

where \mathbf{T} is an effective traction that includes both the actual traction and the effects of the displacement term in (A8) mapped into a traction. Taking \mathbf{T} in the form

$$T_i = \delta \tau_{ij} n_j \quad (A10)$$

with components defined in terms of the stress glut $\delta \tau_{ij}$ of Backus and Mulcahy (1976), one arrives at an expression (A9) that is equivalent to equation (3.26) in Aki and Richards (1980, p. 58). We can use the representation (A9) to compute the range change determined from interferometric synthetic aperture radar (InSAR) data, where the look vector is given by $\mathbf{l} = (l_1, l_2, l_3)$. The range change, $d(\mathbf{x})$, is the projection of the three-dimensional displacement along the look vector (Ferretti 2014) which is given in terms of a summation over the integrals in (A9),

$$d(\mathbf{x}) = \mathbf{u} \cdot \mathbf{l} = l_k \int_{S+S_\sigma} T_i(\boldsymbol{\xi}) G_{ki}(\mathbf{x}, \boldsymbol{\xi}) d\xi. \quad (A11)$$

For a traction vector resulting from forces produced by fluid-induced volume change the primary traction will be a force normal to the local surface denoting the boundary of the reservoir, so that

$$\mathbf{T} = T \mathbf{n} \quad (A12)$$

where T is the magnitude of the traction vector. Hence, we can write (A11) as

$$d(\mathbf{x}) = l_k \int_{S+S_\sigma} T(\boldsymbol{\xi}) n_i G_{ki}(\mathbf{x}, \boldsymbol{\xi}) d\xi. \quad (A13)$$

Defining the kernel

$$K(\mathbf{x}, \boldsymbol{\xi}) = n_i l_k G_{ki}(\mathbf{x}, \boldsymbol{\xi}) \quad (A14)$$

the integral (A13) can be written as

$$d(\mathbf{x}) = \int_{S+S_\sigma} T(\boldsymbol{\xi})K(\mathbf{x}, \boldsymbol{\xi})d\boldsymbol{\xi}. \quad (\text{A15})$$

The forward problem, in which tractions on the source surface S_σ are specified and the displacements or range change at the observation points $d(\mathbf{x})$ are calculated, may be solved by evaluating the integral (A15) explicitly. However, that approach requires a complete specification of the Green's function $G_{ki}(\mathbf{x}, \boldsymbol{\xi})$ which can be a difficult task. Alternatively, we can compute the range change at the Earth's surface using a purely numerical solution of the governing partial differential equations, such as equation (1) or equations (2) and (3). Specifically, one specifies the tractions over the source surface S_σ and uses them to drive the deformation of the numerical simulation.

Based upon equation (A7) we can also define the adjoint operators associated with static and quasi-static deformation. That is, using the linearity of adjoints (Dorny 1983, p. 293) and property (A7), we can express the adjoint of $K(\mathbf{x}, \boldsymbol{\xi})$ given in (A14) as

$$K^*(\mathbf{x}, \boldsymbol{\xi}) = n_i l_k G_{ik}(\boldsymbol{\xi}, \mathbf{x}). \quad (\text{A16})$$

The adjoint integral operator maps range change on S to normal traction on S_σ and is given by

$$\mathcal{T}(\boldsymbol{\xi}) = \int_S \mathcal{D}(\mathbf{x})K^*(\mathbf{x}, \boldsymbol{\xi})d\mathbf{x}. \quad (\text{A17})$$

As with the forward problem, we can evaluate the expression (A17) using a numerical code such as finite-differences. In this case, the simulation computes the normal tensile force at point $\boldsymbol{\xi}$ on the surface of the source region S_σ , due to a distribution of range change over the surface S .

5.3 A discrete formulation

Given that one has a limited set of observations, it is only possible to determine a finite set of parameters or an average of a continuous set. We can formulate a discrete inverse problem directly from the integral expression for the range change, equation (A15) given above. First, consider a set of N observations at discrete points, \mathbf{x}_k , in the case of InSAR gathered at the Earth's surface. Next, partition the surface of integration, S_σ , into a set of sub-patches, thus converting the integration into a summation of integrals over each sub-patch. If desired, the grids used in the numerical solution of the forward problem may be used to define the boundary patches. For example, in our application we will use our finite difference grid to divide the upper surface of the layer of blocks representing the aquifer or reservoir into a set of M rectangular surface patches, with each patch denoted as S_l . Then the integral (A15) for the range at location \mathbf{x}_k , may be written as

$$d(\mathbf{x}_k) = \sum_{l=1}^M A_{kl}m_l \quad (\text{A18})$$

where

$$A_{kl} = \int_{S_l} K(\mathbf{x}_k, \boldsymbol{\xi})d\boldsymbol{\xi} \quad (\text{A19})$$

and m_l is the average normal traction acting on the surface of the l -th grid block.

Because the source acts over a volume, particularly for an aquifer or reservoir model, it is typically defined by an upper and lower surface. Other models, such as vertical or dipping fracture sources, may be bounded by tilted or curved surfaces. In order to reduce the non-uniqueness that is associated with trade-offs between the tractions on paired surface patches, we can assume that the tractions on the two patches are equal. For example, surface elements on the left and right sides of a vertical fracture will be assumed to be subject to equal and opposite tractions. This appears to be a good approximation for fractures and reservoirs where fluid pressures are equalized over their widths. For larger reservoirs, perhaps many grid blocks in thickness, it may be possible to neglect the effect of the lower reservoir/aquifer boundary if it is significantly deeper than the upper boundary. That is the size of the surface deformation due to the traction on the lower boundary may be much smaller than that due to the upper boundary. Numerical testing may be required in order to determine if this is a reasonable approximation.

For a reservoir defined by an upper and lower boundary we can pair up the surface patches for a particular location, defining columns through the reservoir with upper and lower boundaries. We will assume that the reservoir boundaries extend to the edges of the model and that the tractions on the vertical boundaries, at the edge of the model domain, are zero. Assuming that the tractions on the top and bottom boundaries of each column are equal but acting on opposing surface patches, we can still write an expression for the range change at \mathbf{x}_k as the sum

$$d(\mathbf{x}_k) = \sum_{l=1}^M A_{kl}m_l. \quad (\text{A20})$$

But now the sum is over all of the M columns defining the reservoir volume and the coefficients contain two contributions

$$A_{kl} = \int_{U_l} K(\mathbf{x}_k, \boldsymbol{\xi})d\boldsymbol{\xi} + \int_{L_l} K(\mathbf{x}_k, \boldsymbol{\xi})d\boldsymbol{\xi} \quad (\text{A21})$$

from the upper, U_l , and lower, L_l boundary patches of each column. As a related alternative, we could formulate the source in terms of the volumetric component of the stress tensor or as an equivalent pressure change as noted in (Aki and Richards 1980) and (Ichihara et al. 2016).

6 APPENDIX B: AN EXPRESSION FOR THE GRADIENT IN TERMS THE ADJOINT

In this Appendix we develop an expression for the gradient of the misfit functional, following the approach of (Plessix 2006) but only considering the linear forward and inverse problems. This more formal approach complements and supports our Green's function-based discussion in Appendix A.

For the linear forward problem the observable quantities, $\mathbf{u}(\mathbf{m})$, calculated for a specified set of model parameters, with \mathbf{m} satisfy the forward problem $\mathbf{F}(\mathbf{u}(\mathbf{m}), \mathbf{m})$ given by

$$\mathbf{F}(\mathbf{u}, \mathbf{m}) = \mathbf{u} - \mathbf{A}\mathbf{m} = 0. \quad (B1)$$

The misfit functional $J(\mathbf{m})$ is the quadratic least-squares functional

$$J(\mathbf{m}) = h(\mathbf{u}(\mathbf{m}), \mathbf{m}) = \frac{1}{2}(\mathbf{d} - \mathbf{u})^T(\mathbf{d} - \mathbf{u}) \quad (B2)$$

describing the sum of the squares of the differences between the calculated values $\mathbf{u}(\mathbf{m})$ and the vector of observations \mathbf{d} . We consider a perturbation of the model

$$\tilde{\mathbf{m}} = \mathbf{m} + \delta\mathbf{m}, \quad (B3)$$

leading to a perturbation in the values predicted by the forward model

$$\tilde{\mathbf{u}} = \mathbf{u} + \delta\mathbf{u} \quad (B4)$$

with the pair $\tilde{\mathbf{m}}$ and $\tilde{\mathbf{u}}$ satisfying (B1)

$$\mathbf{F}(\tilde{\mathbf{u}}, \tilde{\mathbf{m}}) = \mathbf{F}(\mathbf{u}, \mathbf{m}) + \nabla_{\mathbf{u}}\mathbf{F} \cdot \delta\mathbf{u} + \nabla_{\mathbf{m}}\mathbf{F} \cdot \delta\mathbf{m} = 0. \quad (B5)$$

Since the unperturbed model also satisfies the forward problem, the first term on the right-hand-side of equation (B5) vanishes and we can use the expression to derive a relationship between perturbations in \mathbf{u} and \mathbf{m}

$$\nabla_{\mathbf{u}}\mathbf{F} \cdot \delta\mathbf{u} = -\nabla_{\mathbf{m}}\mathbf{F} \cdot \delta\mathbf{m} \quad (B6)$$

which takes the form

$$\delta\mathbf{u} = \mathbf{A}\delta\mathbf{m} \quad (B7)$$

for our linear forward problem (B1).

Similarly, consider the misfit functional associated with the perturbed model

$$J(\mathbf{m} + \delta\mathbf{m}) = J(\mathbf{m}) + \nabla_{\mathbf{u}}h \cdot \delta\mathbf{u} + \nabla_{\mathbf{m}}h \cdot \delta\mathbf{m} \quad (B8)$$

or

$$\delta J = \nabla_{\mathbf{u}}h \cdot \delta\mathbf{u} + \nabla_{\mathbf{m}}h \cdot \delta\mathbf{m}. \quad (B9)$$

For the quadratic misfit functional (B2) the gradients are given by

$$\nabla_{\mathbf{u}}h = -(\tilde{\mathbf{d}} - \mathbf{u}) \quad (B10)$$

and

$$\nabla_{\mathbf{m}}h = 0 \quad (B11)$$

and equation (B9) takes the form

$$\delta J = -(\tilde{\mathbf{d}} - \mathbf{u}) \cdot \delta\mathbf{u}. \quad (B12)$$

Solving equation (B6) for $\delta\mathbf{u}$ and substituting the expression into (B9) gives

$$\delta J = -\langle \nabla_{\mathbf{u}}h, (\nabla_{\mathbf{u}}\mathbf{F})^{-1} \nabla_{\mathbf{m}}\mathbf{F}\delta\mathbf{m} \rangle + \nabla_{\mathbf{u}}h \cdot \delta\mathbf{m} \quad (B13)$$

where we have written the second scalar product in (B9) using the angle bracket notation used in equation (18). Using the definition (18) of the adjoint we can produce an alternative expression for the quantity in angular brackets in equation (B13)

$$\delta J = -\langle [(\nabla_{\mathbf{u}}\mathbf{F})^{-1}]^* \nabla_{\mathbf{u}}h, \nabla_{\mathbf{m}}\mathbf{F}\delta\mathbf{m} \rangle + \nabla_{\mathbf{m}}h \cdot \delta\mathbf{m} \quad (B14)$$

For the linear forward problem (B1) we have that

$$\nabla_{\mathbf{u}}\mathbf{F} = \mathbf{I} \quad (B15)$$

where \mathbf{I} is the identity matrix, leading to

$$[(\nabla_{\mathbf{u}}\mathbf{F})^{-1}]^* = \mathbf{I}, \quad (B16)$$

in addition to

$$\nabla_{\mathbf{m}}\mathbf{F} = \mathbf{A}. \quad (B17)$$

While the quadratic misfit function (B2) gives

$$\nabla_{\mathbf{u}}h = \mathbf{d} - \mathbf{u} \quad (B18)$$

and

$$\nabla_{\mathbf{m}}h = 0 \quad (B19)$$

leading to the vanishing of the second term on the right-hand-side of equation (B14). The final expression for δJ for the linear inverse problem with the quadratic misfit functional is

$$\delta J = -\langle \mathbf{r}, \mathbf{A}\delta\mathbf{m} \rangle. \quad (B20)$$

where $\mathbf{r} = \mathbf{d} - \mathbf{u}$ is the residual vector introduced in equation (16). Using the definition of the adjoint [see equation (18)] we can write this equation as

$$\delta J = -\langle \mathbf{A}^* \mathbf{r}, \delta\mathbf{m} \rangle. \quad (B21)$$

Figure Captions

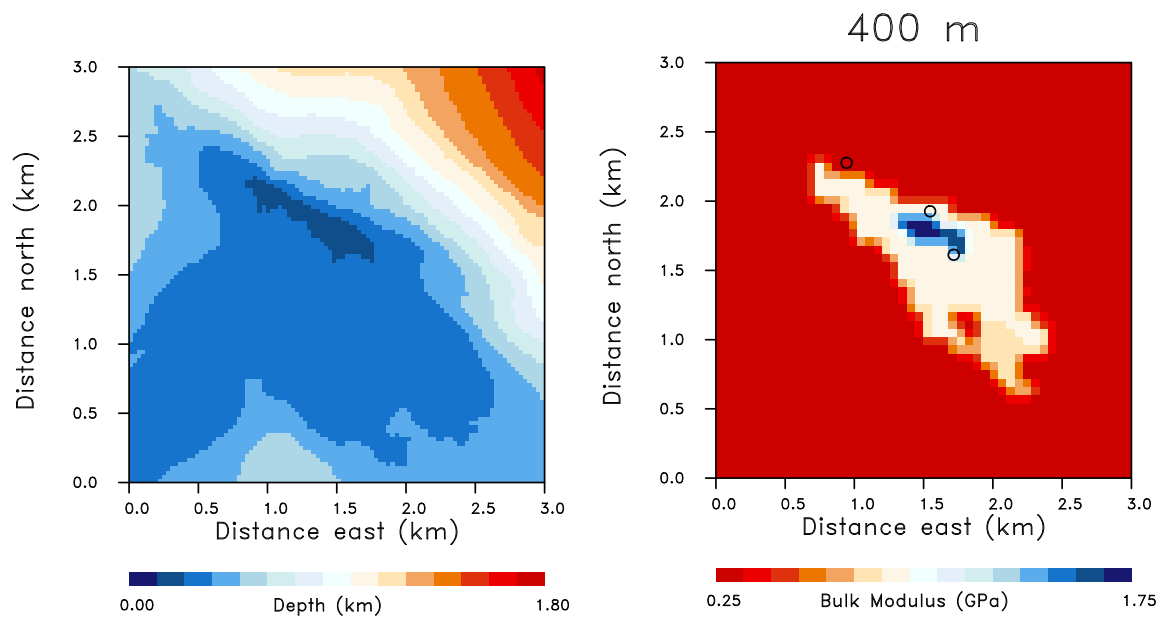


Figure 1. (Left panel) Upper structural boundary of the reservoir, which is defined by a northwest trending anticline. The depths are relative to the top of the anticline. (Right panel) Variations in bulk modulus for a horizontal slice through the model representing the elastic properties of the field.

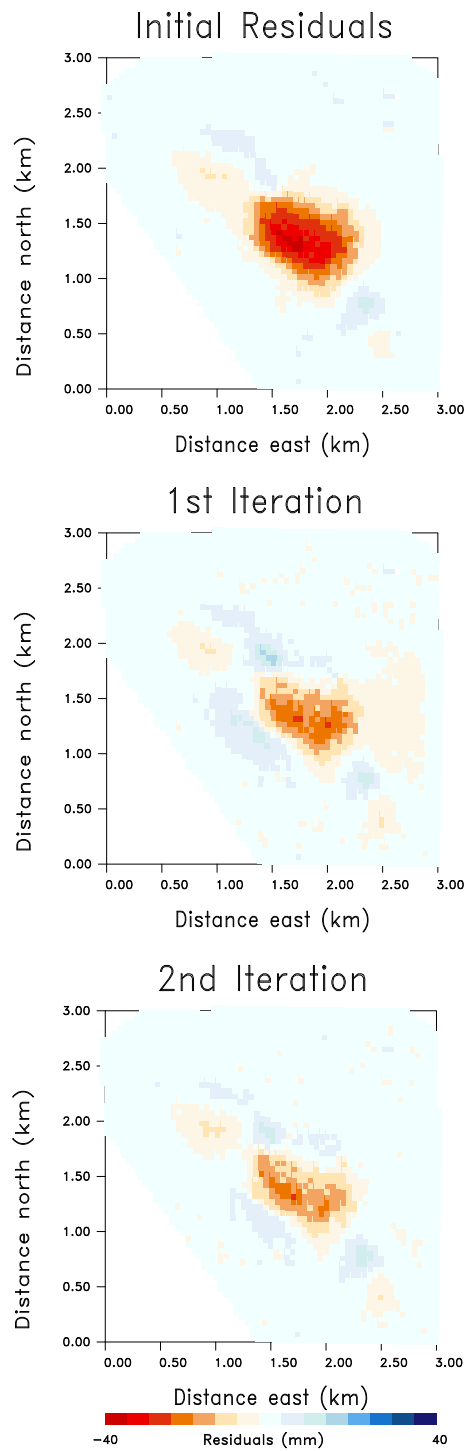


Figure 2. Results for the initial gradients, computed using a homogeneous elastic model. (Top panel) Initial line-of-sight residuals at the start of the conjugate gradient algorithm, for a reservoir model with no active sources. (Center panel) Results for the gradients after the first model update, computed using a homogeneous elastic model. (Bottom panel) Results for the gradients after the second model update, computed using a homogeneous elastic model.

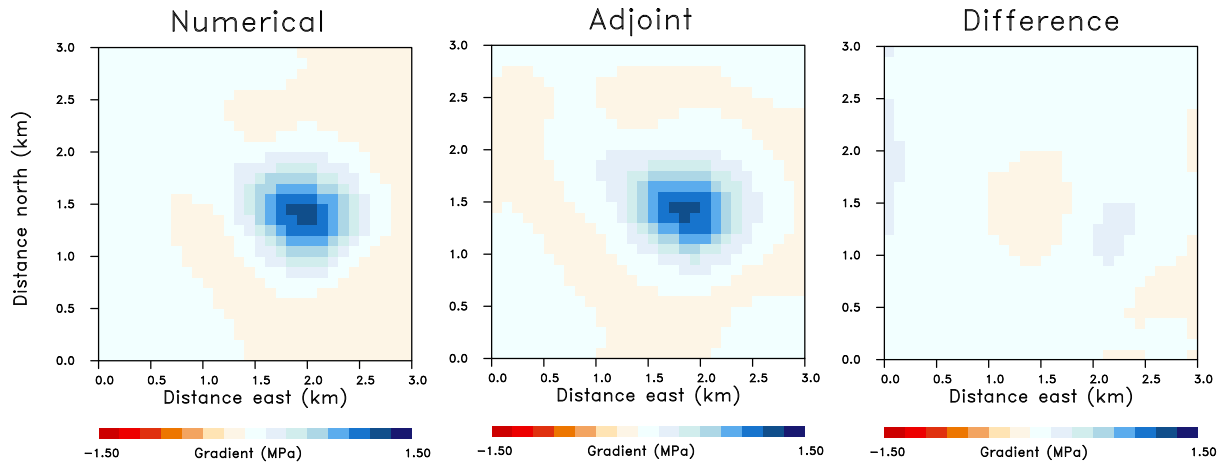


Figure 3. Results for the initial gradients, computed using a homogeneous elastic model. (Left panel) Gradient components obtained using numerical differencing to compute the elements of \mathbf{A} and then using equation (16) to compute $\nabla_m J$. (Center panel) Components of the gradient $\nabla_m J$ computed using the adjoint approach described by equation (18), in which the residuals are used in the simulation to drive the deformation from the observation locations and the gradient estimates are the volumetric stress changes associated with the source grid blocks. (Right panel) Difference between the numerical gradient estimates and the adjoint-based estimates.

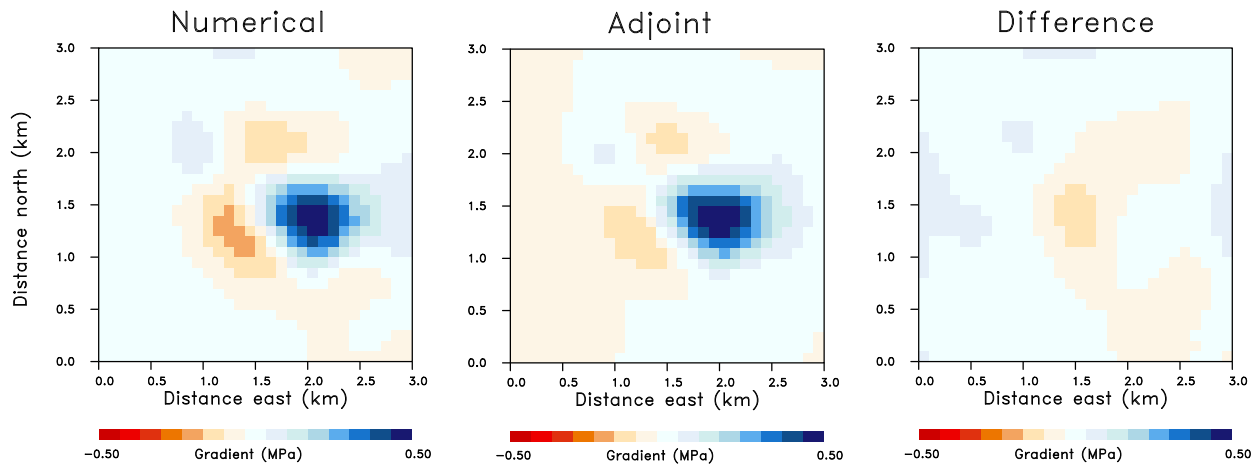


Figure 4. Results for the gradients after the first model update, computed using a homogeneous elastic model. (Left panel) Gradient components calculated using conventional approach based upon equation (16). (Center panel) Adjoint-based gradient estimates corresponding the the residuals in the Left panel. (Right panel) Differences obtained by subtracting the adjoint-based gradient estimates from the numerical gradient estimates.

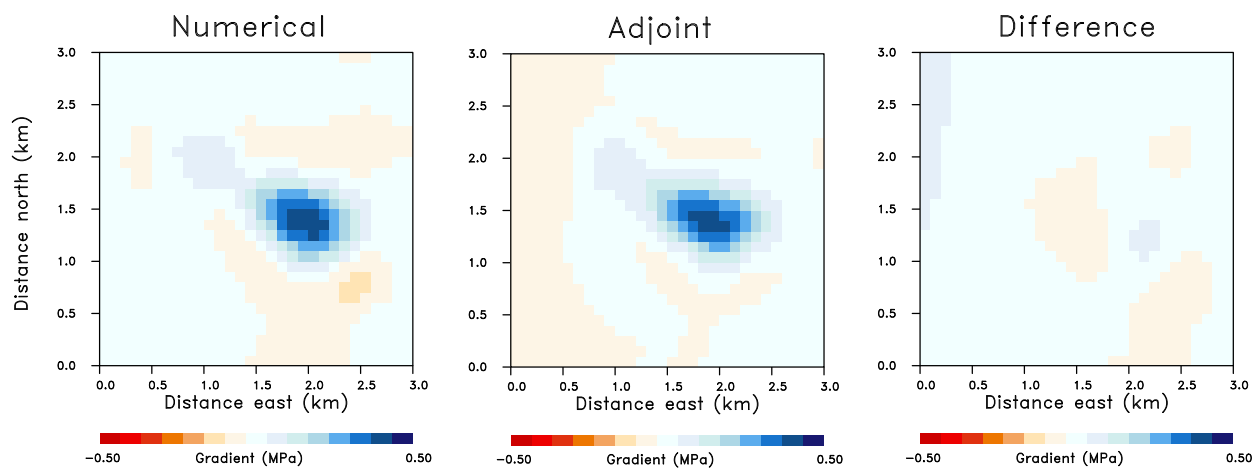


Figure 5. Second iteration of the conjugate gradient model update. (Left panel) Gradient components estimated using the numerical differencing approach. (Center panel) Gradient component derived using the adjoint approach. (Right panel) Differences between the two sets of gradient estimates.

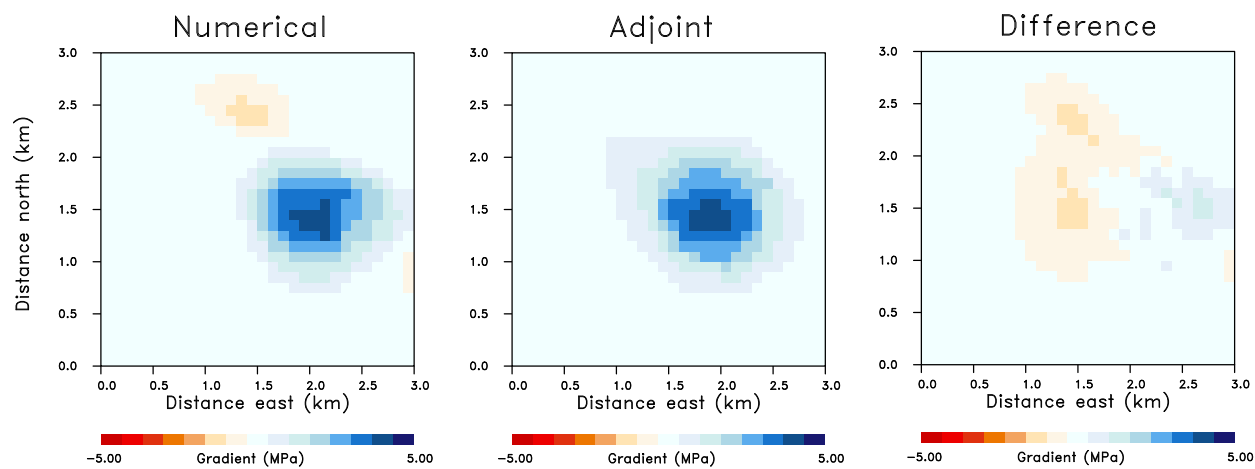


Figure 6. Gradient calculations based upon the three-dimensional model for the Central Valley oil field. The elements of the gradient are associated with the starting or initial model of the conjugate gradient algorithm. (Left panel) Gradient components computed using the conventional numerical approach. (Center panel) Adjoint-based estimates of the components of the gradient vector. (Right panel) Gradient difference between the two sets of estimates.

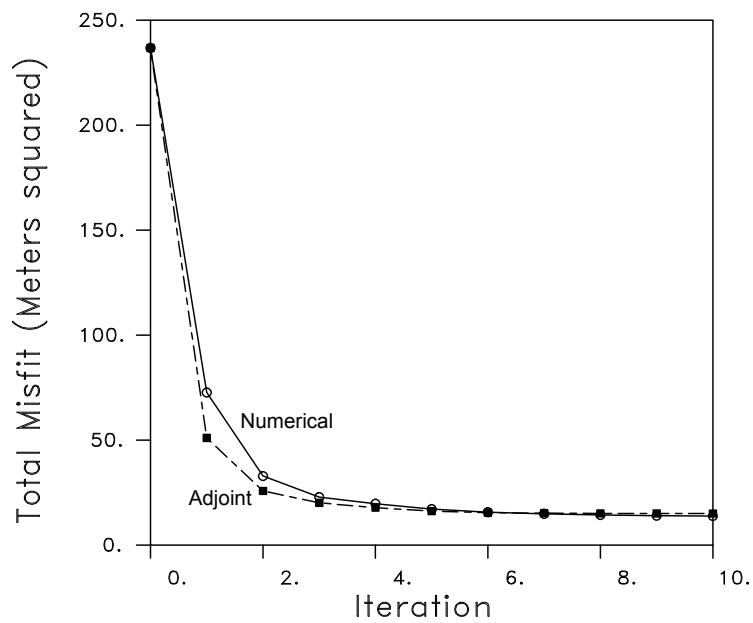


Figure 7. Reduction in square root of the total sum of the squares of the residuals as a function of the iterations of the conjugate gradient algorithm. Both the error reduction associated with the numerical and adjoint approaches are plotted.

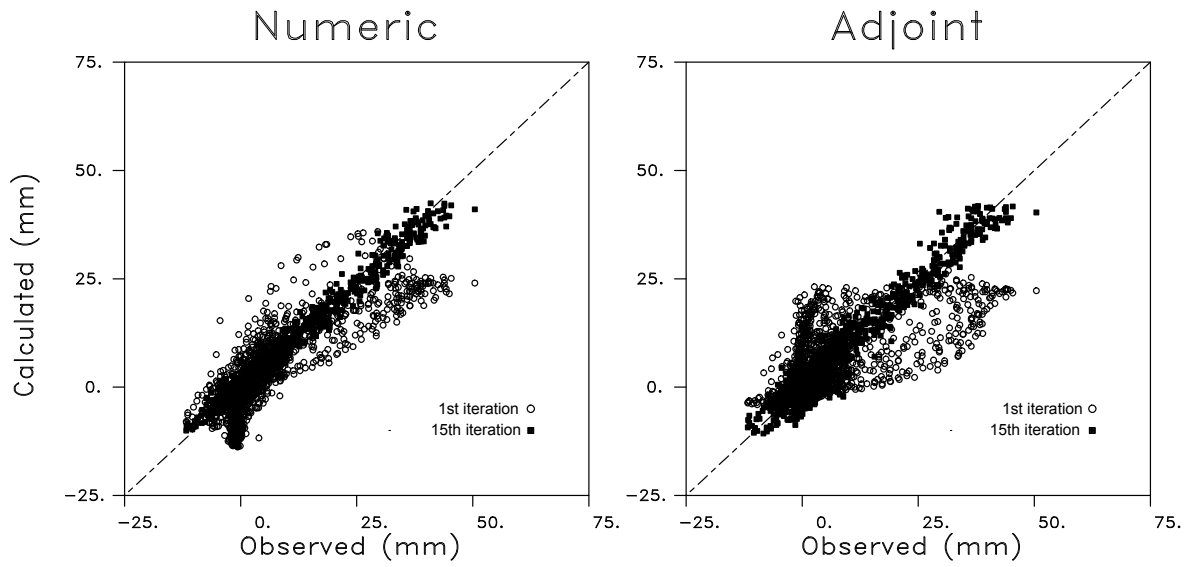


Figure 8. Calculated line-of-sight displacements plotted against observed values for (Left panel) the conjugate gradient algorithm utilizing numerical gradient components and (Right panel) a conjugate gradient algorithm based upon gradient components calculated using adjoints. Estimates calculated at the first (open circles) and final (filled black squares) iterations are plotted in each panel.

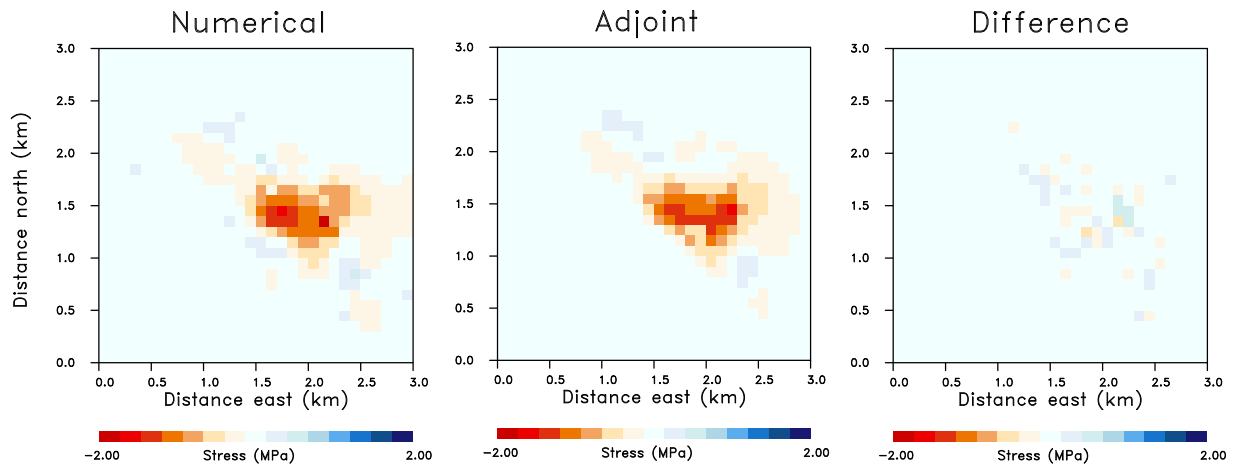


Figure 9. Final models of reservoir boundary normal stresses from the conjugate gradient algorithms. (Left panel) Model produced by the conjugate gradient scheme with conventional numerical gradient estimates. (Center panel) Final model from the adjoint-based conjugate gradient inversion. (Right panel) Difference between the two models resulting from subtracting the adjoint solution from the numerical solution.

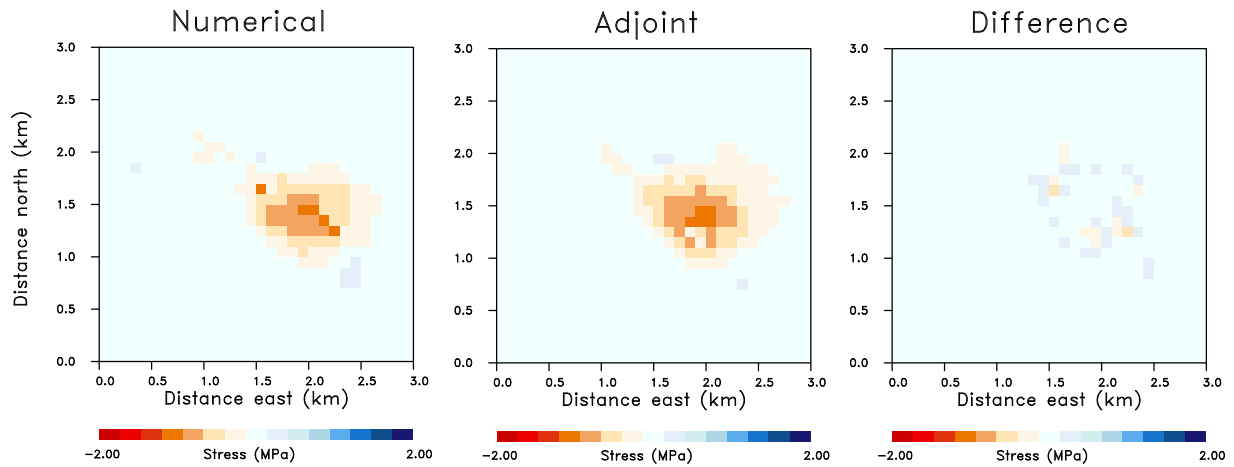


Figure 10. Models resulting from an inversion of a sparse data set obtained by re-interpolating the 2986 observed values onto a 20 by 20 grid of range changes. (Left panel) Model produced by the conjugate gradient scheme with conventional numerical gradient estimates. (Center panel) Final model from the adjoint-based conjugate gradient inversion. (Right panel) Difference between the two models resulting from subtracting the adjoint solution from the numerical solution.